

# Cubic Nonlinearity Driven Up-Conversion in High-Field Plasmonic Hot Carrier Systems

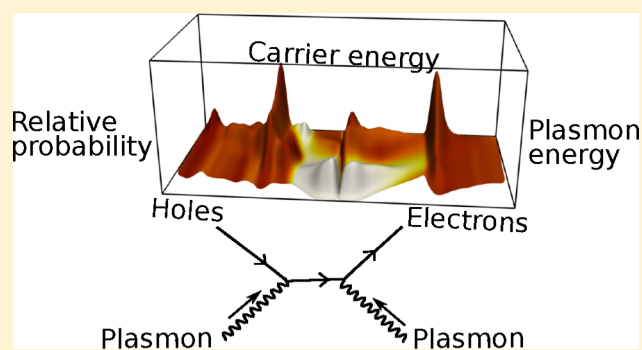
Prineha Narang,<sup>\*,†,‡,§,||</sup> Ravishankar Sundararaman,<sup>\*,†,§</sup> Adam S. Jermyn,<sup>⊥,#</sup> William A. Goddard, III,<sup>§,○</sup> and Harry A. Atwater<sup>\*,‡,§</sup>

<sup>‡</sup>Thomas J. Watson Laboratories of Applied Physics, <sup>§</sup>Joint Center for Artificial Photosynthesis, <sup>⊥</sup>Division of Physics, Mathematics and Astronomy, and <sup>○</sup>Materials and Process Simulation Center, California Institute of Technology, 1200 East California Boulevard, Pasadena, California 91125, United States

<sup>||</sup>NG NEXT, 1 Space Park Drive, Redondo Beach, California, United States

<sup>#</sup>Institute of Astronomy, Cambridge University, Cambridge, United Kingdom CB3 0HA

**ABSTRACT:** Surface plasmon resonances confine electromagnetic fields to the nanoscale, producing high field strengths suitable for exploiting nonlinear optical properties. We examine the prospect of detecting and utilizing one such property in plasmonic metals: the imaginary part of the cubic susceptibility, which corresponds to two plasmons decaying together to produce high energy carriers. Here we present ab initio predictions of the rates and carrier distributions generated by direct interband and phonon-assisted intraband transitions in one and two-plasmon decay. We propose detection of the higher energy carriers generated from two-plasmon decays that are inaccessible in one-plasmon decay as a viable signature of these processes in ultrafast experiments.



## INTRODUCTION

Plasmonic systems are promising for manipulating light at the nanoscale.<sup>1–3</sup> By confining light within tens of nanometers of the surface, surface plasmon polaritons (SPPs) enhance light–matter interactions and make it possible to access nonlinear effects.<sup>4</sup> Centrosymmetric materials such as face-centered and body-centered cubic metals do not possess intrinsic quadratic nonlinearities. Nevertheless, these metals display an effective second order nonlinearity that arises from symmetry breaking at the surface,<sup>5,6</sup> which is inevitable in plasmonics. They also possess intrinsic third order nonlinearities detectable in the optical response.<sup>7–9</sup> High-intensity light, such as from a femtosecond optical pulse, incident on the metal surface perturbs the energy-momentum distribution of electrons from equilibrium, thereby influencing SPP propagation and introducing effective two-plasmon interactions. The complexity of such nonlinear processes, both for localized plasmons and propagating SPPs, necessitates the development of general theoretical and computational techniques to aid experiment analysis as well as to provide a deeper insight into the involved physics.

A wide variety of applications stem from these higher-order plasmonic processes. Devices with ultrafast femtosecond switching times and modest switching energy requirements may be achieved by leveraging nonlinear plasmonics and active plasmonic switching.<sup>10</sup> Nonlinear plasmonic phenomena also find potential applications in energy systems and catalysis, including plasmonic heating and hot carrier up-conversion in

plasmon decay.<sup>11–14</sup> The latter process involving the cooperative decay of multiple plasmons to high energy carriers could find applications in surface spectroscopy, surface chemistry, or other imaging techniques enhanced by plasmonic interactions.<sup>15–17</sup> The microscopic mechanisms in plasmon decays (to carriers and eventually heat) across various energy, length, and time scales are still a subject of considerable debate.<sup>18–21</sup> Carriers generated from plasmon decay have been shown to drive high-barrier chemical reactions, both directly on the metal surface<sup>22</sup> and via resonant energy transfer to semiconductors.<sup>23</sup> An open question in plasmonic catalysis is the possibility of driving difficult reactions using up-converted carriers with higher energy from two or more plasmons decaying together, which we address in this Article.

Here we focus on the cubic susceptibility  $\chi_3$ , since it is an intrinsic fundamental property of the material (unlike  $\chi_2$ , which is a surface/geometric property). The cubic nonlinearity in metals is much larger than in semiconductors, especially at low frequencies, due to the Drude response divergence at zero frequency. An important question is whether the nonlinearity is conservative ( $\text{Re } \chi^3$ ) or dissipative ( $\text{Im } \chi^3$ ). Directly measuring the inherent metal nonlinear susceptibility, especially with

**Special Issue:** Richard P. Van Duyne Festschrift

**Received:** April 5, 2016

**Revised:** June 20, 2016

phase information, to answer the above question is somewhat challenging. Numerous experiments measure the optical response of nanoparticle composites and deduce the metal nonlinear susceptibility indirectly using predictions from effective medium theory.<sup>24</sup> On the other hand, *z*-scan experiments on metal films<sup>25</sup> lead to values of  $\chi^3$  different than those extracted from composites.<sup>7,26</sup> Ultrafast experiments also have been used to estimate the cubic optical nonlinearity in bulk gold,<sup>27</sup> but so far these estimates are indirect, depend on assumptions about laser pulse durations and excited carrier lifetimes, and are extremely sensitive to instantaneous intensity.<sup>6,28</sup>

Previous theories also propose measurements of surface plasmon polariton collisions.<sup>29–31</sup> More fundamentally, since surface plasmons are electromagnetic modes (photons) confined to metal surfaces, multiplasmon decay can also be explored using conventional two-photon measurements on plasmonic systems,<sup>32–34</sup> with the distinction between plasmons and photons being on- versus off-resonance. The limit in exploring such measurements currently is that predictions of intrinsic nonlinear optical properties of plasmonic metals and theories of multiplasmon decay or the associated carrier dynamics are not yet available. This Article uses first-principles calculations of the microscopic processes underlying multiplasmon decay to address such questions.

## THEORY

In this work, we focus on the imaginary part,  $\text{Im } \chi^3$ , of the cubic susceptibility for two reasons: First, this corresponds physically to two plasmons (or photons) exciting an electronic transition in the material with the sum of their energies, resulting in higher energy carriers than the corresponding transitions induced by single plasmons which contribute to  $\text{Im } \chi^1$ . This opens up the unique possibility of electrically detecting the two-plasmon process by distinguishing carrier energies, as we discuss later. Second, the imaginary parts of the susceptibility have a closer connection to the electronic structure properties of the material such as the joint density of states at a given frequency. They are computationally tractable and easier to interpret physically compared to the real parts ( $\text{Re } \chi^3$ ), which require additional frequency integrals in the Kramers–Kronig relations.<sup>35</sup>

We consider processes involving one or two plasmons of the same mode, frequency and polarization, in order to keep manageable the number of variables explored below (material, geometry, frequency, carrier energy, intensity etc.). The extension to plasmons of different modes is straightforward but that does not lend any additional insight, and we therefore omit such cases here for simplicity. With a single plasmon frequency  $\omega$ , the one plasmon process  $\text{Im } \chi^1$  then excites electronic transitions with energy  $\hbar\omega$ , whereas the two-plasmon process excites those with energy  $2\hbar\omega$ .

Previously we analyzed the one-plasmon process ( $\text{Im } \chi^1$ ) in great detail<sup>36</sup> and showed that we can quantitatively account for experimental decay rates with first-principles calculations of direct and phonon-assisted transitions. Figure 1 shows the Feynman diagrams associated with these processes. The direct transition absorbs a plasmon and creates an electron–hole pair with net zero crystal momentum, which is possible only above the interband threshold energy  $E_t$ . Direct transitions dominate above this threshold and are forbidden below it. Below threshold,  $\text{Im } \chi^1$  is dominated by phonon-assisted intraband transitions, which derive momentum from the additional

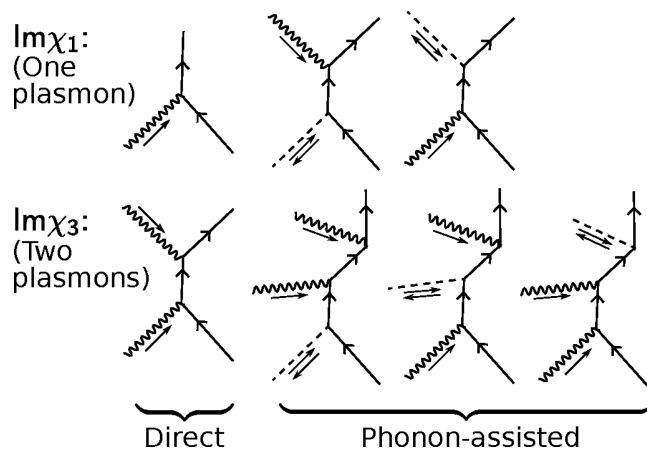


**Figure 1.** Feynman diagram representation of single and two-plasmon processes that correspond to  $\text{Im } \chi^1$  and  $\text{Im } \chi^3$ , respectively.  $\text{Re } \chi^3$  is the conservative response, whereas  $\text{Im } \chi^3$  is the dissipative response of the material. Both direct and phonon-assisted processes are important to capture the dominant processes at all frequencies.

absorption or emission of phonons to excite an electron–hole pair with net crystal momentum. Fermi’s golden rule for the contributions due to the Feynman diagrams shown in Figure 1 yields<sup>36</sup>

$$\begin{aligned} \text{Im } \chi_{\text{direct}}^1(\omega) &= \frac{\pi e^2}{\omega^2} \int_{\text{BZ}} \frac{d\mathbf{q}}{(2\pi)^3} \sum_{n'n} (f_{q_n} - f_{q_n'}) \delta(\epsilon_{q_n'} - \epsilon_{q_n} - \hbar\omega) \\ &\times |\hat{\mathbf{E}} \cdot \langle \mathbf{v} \rangle_{n'n}^q|^2, \text{ and} \\ \text{Im } \chi_{\text{phonon}}^1(\omega) &= \frac{\pi e^2}{\omega^2} \int_{\text{BZ}} \frac{d\mathbf{q}' d\mathbf{q}}{(2\pi)^6} \sum_{n'n'\alpha\pm} (f_{q_n} - f_{q_n'}) \left( n_{q'-q,\alpha} + \frac{1}{2} \mp \frac{1}{2} \right) \\ &\times \delta(\epsilon_{q_n'} - \epsilon_{q_n} - \hbar\omega \mp \hbar\omega_{q'-q,\alpha}) \\ &\times \left| \hat{\mathbf{E}} \cdot \sum_{n_1} \left( \frac{\langle \mathbf{v} \rangle_{n_1 n_1}^{q'} g_{q' n_1, q_n}^{q'-q,\alpha}}{\epsilon_{q' n_1} - \epsilon_{q_n'} + \hbar\omega + i\eta} + \frac{g_{q' n_1, q_n}^{q'-q,\alpha} \langle \mathbf{v} \rangle_{n_1 n_1}^q}{\epsilon_{q_n} - \epsilon_{q_n'} - \hbar\omega + i\eta} \right) \right|^2 \end{aligned} \quad (1)$$

Here,  $\epsilon_{q_n}$  and  $f_{q_n}$  are the energies and Fermi occupations of electrons with wave-vector  $\mathbf{q}$  (in the Brillouin zone BZ) and band index  $n$ ,  $\hbar\omega_{k\alpha}$  and  $n_{k\alpha}$  are the energies and Bose occupations of phonons with wave-vector  $\mathbf{k}$  and polarization index  $\alpha$ , while  $\langle \mathbf{v} \rangle_{n'n}^q$  and  $g_{q' n_1, q_n}^{k\alpha}$  are electron velocity and electron–phonon matrix elements, respectively. The sum over  $\pm$  accounts for phonon absorption as well as emission. Above,  $\hat{\mathbf{E}}$  is the electric field direction and  $\chi$  is, in principle, a rank-2 tensor that depends on this direction, but we deal here with face-centered cubic metals for which the above expressions are isotropic by symmetry.

We calculate all the above quantities directly from ab initio calculations employing an accurate relativistic DFT+*U* approach.<sup>37</sup> The band indices  $n, n'$  implicitly count spinorial bands so that there is no factor of 2 from spin degeneracy in Fermi’s golden rule, while the electron–plasmon (velocity) and electron–phonon matrix elements explicitly trace over spinorial degrees of freedom in the electronic states. Note that the electron–plasmon matrix element also corresponds to the relativistic  $\mathbf{A} \cdot \mathbf{p}$  gauge coupling, except that we write the vector potential  $\mathbf{A}$  in terms of the electric field  $\mathbf{E}$  in the radiation gauge, and the electron momentum  $\mathbf{p}$  in terms of velocity  $\mathbf{v}$  to simplify prefactors. Also note that we account for all the lowest-order diagrams that contribute to  $\text{Im } \chi^1$  above (and similarly  $\text{Im } \chi^3$  below). Loop diagrams on the propagators are implicitly

approximated in the DFT treatment of electrons and phonons and the dielectric function treatment of plasmons, while we neglect vertex corrections from higher-order loop diagrams. See the [Methods](#) section for a summary of computational parameters and refs 36 and 37 for more details on the theory and approximations.

The two-plasmon process ( $\text{Im } \chi^3$ ), similarly, includes direct and phonon-assisted contributions (see [Figure 1](#)). The lowest order process involves two plasmons decaying together to excite an electronic transition with the sum of their energies. However, the total plasmon momentum is still negligible

compared to electron momenta requiring the initial and final electron states to have the same crystal momentum, which implies that the total energy of the transition must exceed the interband threshold energy  $E_t$ . Therefore, this process dominates above plasmon energies  $E_t/2$ . Again, phonons can provide momentum to excite transitions with different initial and final electron crystal momenta and this process dominates below the two-plasmon threshold energy  $E_t/2$ . Analogously to the one-plasmon case, the Feynman diagrams for these processes evaluate to

$$\text{Im } \chi_{\text{direct}}^3(\omega) = \frac{\pi e^4}{\omega^4} \int_{\text{BZ}} \frac{d\mathbf{q}}{(2\pi)^3} \sum_{n'n} (f_{\mathbf{q}n} - f_{\mathbf{q}n'}) \delta(\varepsilon_{\mathbf{q}n'} - \varepsilon_{\mathbf{q}n} - 2\hbar\omega) \left| \sum_{n_1} \frac{2(\hat{\mathbf{E}} \cdot \langle \mathbf{v} \rangle_{n'n_1}^{\mathbf{q}})(\hat{\mathbf{E}} \cdot \langle \mathbf{v} \rangle_{n_1n}^{\mathbf{q}})}{\varepsilon_{\mathbf{q}n_1} - \varepsilon_{\mathbf{q}n} - \hbar\omega + i\eta} \right|^2, \text{ and} \quad (3)$$

$$\text{Im } \chi_{\text{phonon}}^3(\omega) = \frac{\pi e^4}{\omega^4} \int_{\text{BZ}} \frac{d\mathbf{q}'d\mathbf{q}}{(2\pi)^6} \sum_{n'n\alpha\pm} (f_{\mathbf{q}n} - f_{\mathbf{q}'n'}) \left( n_{\mathbf{q}'-\mathbf{q},\alpha} + \frac{1}{2} \mp \frac{1}{2} \right) \delta(\varepsilon_{\mathbf{q}'n'} - \varepsilon_{\mathbf{q}n} - 2\hbar\omega \mp \hbar\omega_{\mathbf{q}'-\mathbf{q},\alpha})$$

$$\times \left| \sum_{n_1n_2} \left( \frac{(\hat{\mathbf{E}} \cdot \langle \mathbf{v} \rangle_{n'n_2}^{\mathbf{q}'}) (\hat{\mathbf{E}} \cdot \langle \mathbf{v} \rangle_{n_2n_1}^{\mathbf{q}'}) g_{\mathbf{q}'n_1, \mathbf{q}n}^{\mathbf{q}'-\mathbf{q},\alpha}}{(\varepsilon_{\mathbf{q}'n_2} - \varepsilon_{\mathbf{q}'n'} + \hbar\omega + i\eta)(\varepsilon_{\mathbf{q}'n_1} - \varepsilon_{\mathbf{q}'n'} + 2\hbar\omega + i\eta)} + \frac{(\hat{\mathbf{E}} \cdot \langle \mathbf{v} \rangle_{n'n_2}^{\mathbf{q}'}) g_{\mathbf{q}'n_2, \mathbf{q}n_1}^{\mathbf{q}'-\mathbf{q},\alpha} (\hat{\mathbf{E}} \cdot \langle \mathbf{v} \rangle_{n_1n}^{\mathbf{q}})}{(\varepsilon_{\mathbf{q}'n_2} - \varepsilon_{\mathbf{q}'n'} + \hbar\omega + i\eta)(\varepsilon_{\mathbf{q}n_1} - \varepsilon_{\mathbf{q}n} - \hbar\omega + i\eta)} \right) \right|^2 \quad (4)$$

$$+ \frac{g_{\mathbf{q}'n', \mathbf{q}n_2}^{\mathbf{q}'-\mathbf{q},\alpha} (\hat{\mathbf{E}} \cdot \langle \mathbf{v} \rangle_{n_2n_1}^{\mathbf{q}})(\hat{\mathbf{E}} \cdot \langle \mathbf{v} \rangle_{n_1n}^{\mathbf{q}})}{(\varepsilon_{\mathbf{q}n_2} - \varepsilon_{\mathbf{q}n} - 2\hbar\omega + i\eta)(\varepsilon_{\mathbf{q}n_1} - \varepsilon_{\mathbf{q}n} - \hbar\omega + i\eta)}$$

In this case, the direct contributions involve a second-order matrix element with a single sum over intermediate bands ( $n_1$ ), whereas the phonon-assisted contributions involve a third-order matrix element with a double sum ( $n_1, n_2$ ).

The imaginary part,  $\eta$ , of each energy denominator in eqs 2–4 corresponds to the line width of the intermediate electronic state involved in that energy denominator. However, as we discuss in detail in ref 36, the singular on-shell parts of higher order Feynman diagrams in metals involving phonon absorption or emission in the initial or final states count the sequential processes consisting of optical excitation followed or preceded by electron–phonon scattering multiple times. We eliminate this multiple counting by using an extrapolation scheme in  $\eta$  that subtracts only these redundant singular contributions. (See ref 36 for details.) Similarly, in this case, we use the extrapolation scheme for  $\eta$  in eq 2 and in the first and last terms in the matrix element of eq 4 so as to not count redundant sequential processes. On the other hand, eq 3 and the second term in the matrix element of eq 4 correspond to physically meaningful sequential two-plasmon decay, so we set  $\eta$  to the corresponding intermediate electron line width in those terms. In all cases, the sum of the initial and final electron line width sets the width of the energy-conserving delta-function (from Fermi's golden rule). We calculate these electron line widths ab initio as well, using Fermi's golden rule for electron–electron and electron–phonon scattering contributions. The calculated line widths depend on electron energy and band index; we use these state-dependent values directly in the above expressions. See ref 36 for details of these scattering calculations and plots of the carrier lifetimes ( $\hbar/(2$  line width)) as a function of energy.

## RESULTS

[Figure 2](#) shows the cumulative contributions of direct and phonon-assisted processes to  $\text{Im } \chi^1$  and  $\text{Im } \chi^3$  for aluminum and the noble metals. Direct transitions dominate  $\text{Im } \chi^1$  above the interband threshold for  $d \rightarrow s$  transitions at approximately 2 eV for copper and gold and 3.5 eV for silver. In aluminum,

direct transitions are allowed at all energies, but dominate only above a threshold energy of approximately 1.6 eV. Phonon-assisted intraband transitions dominate below these threshold energies, and the cumulative contributions agree very well with experimental measurements (ellipsometry) for all four metals.<sup>36</sup> The DFT predictions are typically within 50% of reported measurements, which is better than the agreement between different measurements of the dielectric functions of plasmonic metals.<sup>38</sup> The dominant errors in our predicted  $\text{Im } \chi^3$  are due to small discrepancies in the DFT+*U* positions of the *d*-bands in the noble metals (aluminum without *d* bands shows much better agreement), and we expect similar relative accuracy in our predictions for  $\text{Im } \chi^3$  below. These accuracies could be improved, in principle, by performing GW quasiparticle band structure calculations,<sup>39</sup> but the correct approach for such calculations of metals is not yet clear,<sup>40</sup> and so far, our DFT+*U* band structures have proven to compare best with experimental measurements.<sup>37</sup>

Qualitatively,  $\text{Im } \chi^3$  exhibits a similar frequency dependence in all cases, except that the energy scale is halved since two plasmons combine to excite the transition: direct transitions are allowed and dominate above half the interband threshold energy, while phonon-assisted intraband transitions dominate below it. Measuring  $\text{Im } \chi^3$  of plasmonic metals is challenging because the field inside the metals is much smaller than external fields making it difficult to reliably access the nonlinear regime in continuous wave measurements. Few estimates of this quantity are available from pump–probe pulsed laser measurements such as ref 27 for gold, which finds  $\chi^3 \sim 7 \times 10^{-9}$  esu  $\sim 2 \times 10^6$  au for 1 eV photons, which agrees reasonably with the ab initio predictions shown in [Figure 2](#), within the relative accuracy discussed for  $\text{Im } \chi^1$  above.

As discussed above,  $\text{Im } \chi^1$  and  $\text{Im } \chi^3$  are losses that correspond to exciting carriers in the metal. Experimentally determining the energy distributions of the generated carriers is extremely challenging, but ab initio calculations provide this information directly. The integrands in eqs 1–4 each correspond to an electronic transition that leaves a hole behind

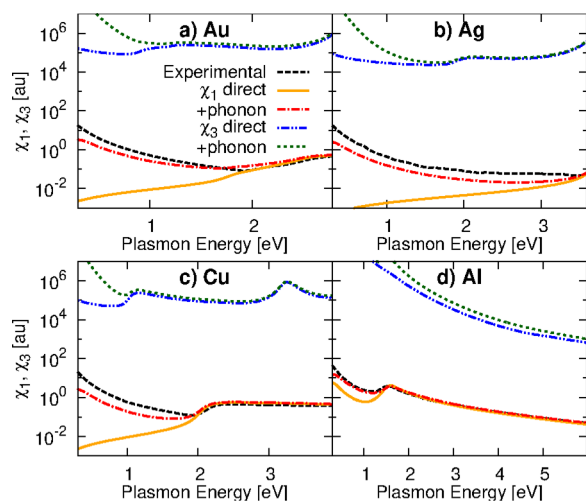


**Figure 2.** Comparison of contributions to linear and cubic susceptibilities,  $\text{Im } \chi^1$  and  $\text{Im } \chi^3$ , as a function of frequency in (a) gold, (b) silver, (c) copper, and (d) aluminum. Direct transitions dominate  $\text{Im } \chi^1$  above the interband threshold energy  $E_t$  and  $\text{Im } \chi^3$  above  $E_t/2$ . The lines labeled ‘+phonon’ show the total contributions from direct and phonon-assisted transitions, and the latter dominate  $\text{Im } \chi^1$  and  $\text{Im } \chi^3$  below  $E_t$  and  $E_t/2$  respectively. The experimental estimates for  $\text{Im } \chi^1$  are obtained from ellipsometry.<sup>38</sup> Note that  $\chi^1$  is dimensionless, and we plot  $\chi^3$  in atomic units where  $1 \text{ au} = (\text{e-bohr}/\text{Hartree})^2 \approx 3.8 \times 10^{-24} (\text{m/V})^2 [\text{SI}] \approx 3.4 \times 10^{-15} (\text{cm/statvolt})^2 [\text{ESU}]$ .

of energy  $\varepsilon_{q'n}$  and generates an electron of energy  $\varepsilon_{q'n}$  (or  $\varepsilon_{q'n}$  in the phonon-assisted case). While computing the integrals for  $\text{Im } \chi^1$  and  $\text{Im } \chi^3$ , we histogram the contributions by these electron and hole energies to predict the generated hot carrier distributions. **Figure 3** compares the energy distributions of hot carriers generated by one-plasmon ( $\text{Im } \chi^1$ ) and two-plasmon ( $\text{Im } \chi^3$ ) processes as a function of plasmon energy for the four common plasmonic metals. Below threshold, the phonon-assisted transitions generate flat distributions of electrons and holes extending from zero to the plasmon energy in  $\text{Im } \chi^1$  and to twice the plasmon energy in  $\text{Im } \chi^3$ , seen in the Figure as the light gray plateaus in the foreground. Above threshold, direct  $d \rightarrow s$  transitions produce high energy holes and lower energy electrons in the one-plasmon process in the noble metals, seen in the Figure as the dark red hills in the background. Additionally, transitions between the conduction bands produce low energy holes and high energy electrons in silver; this process is not accessible in one-plasmon processes in copper and gold, but opens up in the two-plasmon processes in all three noble metals. Aluminum exhibits flat distributions of carriers for one and two-plasmon processes despite the contribution of interband transitions, but an additional transition generating predominantly high-energy electrons opens up in the deep ultraviolet at a plasmon energy of  $\sim 5$  eV. The asymmetries between electrons and holes, and the gaps in certain energy and frequency ranges of the carrier energy distributions, are consequences of the selection rule in direct-transitions requiring pairs of states with the same crystal momentum straddling the Fermi level, as discussed in detail previously for the one-plasmon decay process.<sup>36,37</sup>

A key signature of the two-plasmon process seen above is the accessibility of interband transitions at energies far below the one-plasmon process. These transitions specifically generate high-energy electrons or holes, that could inject across high

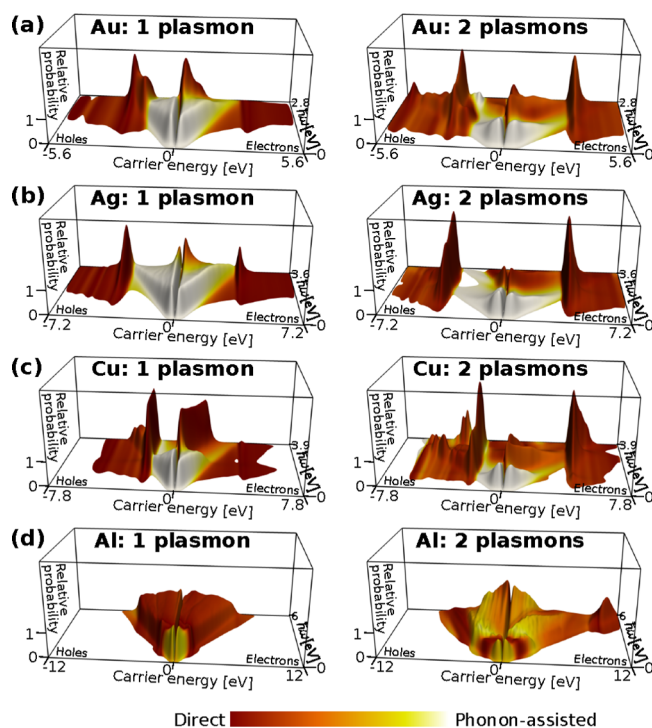


**Figure 3.** Energy distributions of hot electrons and holes generated due to single plasmon decay (left panels) and two-plasmon generated (right panels) in (a) gold, (b) silver, (c) copper, and (d) aluminum. In each panel, the carrier energy varies from left to right and the plasmon energy from front to back. The color scale indicates the relative contributions of direct transitions (dark red) and phonon-assisted transitions (white). The carrier probabilities (vertical axis) are normalized for each plasmon energy such that a uniform distribution would be 1, as seen approximately for the single plasmon results of aluminum and below threshold for the noble metals.

barriers in meta-insulator interfaces, or into energy levels of adsorbed molecules that are far from the Fermi level. With careful selection of adsorbed molecules or functionalizing ligands that only respond to high energy carriers, the latter process could be useful for discerning the two-plasmon process from the one-plasmon process in surface-enhanced Raman or photoluminescence experiments.

So far, we have discussed the frequency dependence of the one and two plasmon processes including the resulting hot carrier distributions excited in the metal. In any given experiment, both types of processes would always occur, but the relative probabilities of the two change with the electric field in the metal, which in turn depends on the incident light intensity and metal geometry. Specifically, the absorbed power, and hence the net hot carrier generation rate, due to the one-plasmon process is proportional to  $\int d\mathbf{r} \text{Im } \chi^1 E^2(\mathbf{r})$ , and that due to the two-plasmon process is proportional to  $\int d\mathbf{r} \text{Im } \chi^3 E^4(\mathbf{r})$ , where  $E(\mathbf{r})$  is the electric field inside the metal. Therefore, the relative contributions of one and two-plasmon processes for a given geometry and incident light intensity depends on the average  $E^2$  and  $E^4$  inside the metal. For simplicity, we consider two prototypical geometries for which the field distributions can be evaluated analytically: the semi-infinite metal slab and a metal sphere. For the slab, we assume a roughened surface with ideal coupling (since a smooth metal surface reflects most of the incident light) and for the sphere we calculate the field profiles and averages using Mie theory.<sup>41,42</sup>

**Figure 4** compares the one- and two-plasmon contributions for the ideal-coupling slab and spheres of two sizes as a function

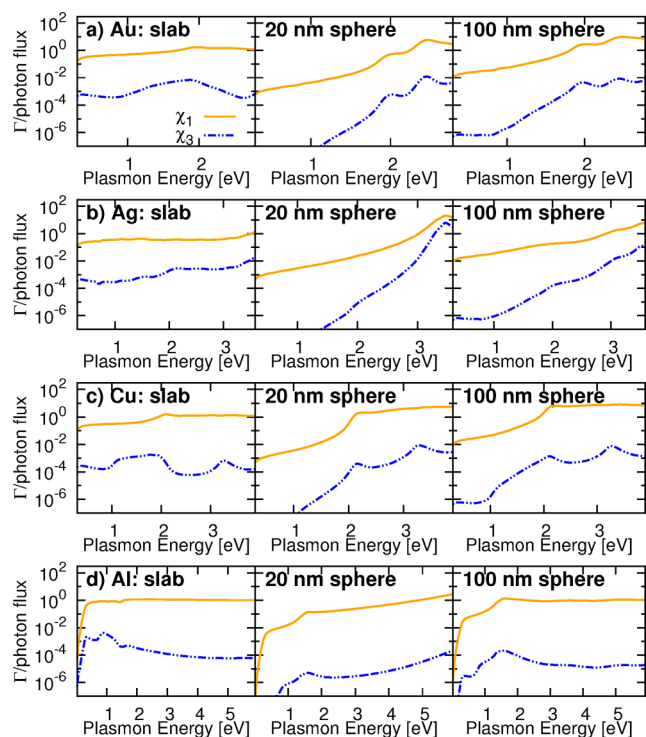


**Figure 4.** One- and two-plasmon decay rates per photon flux for various geometries in (a) gold, (b) silver, (c) copper, and (d) aluminum as a function of plasmon energy at a reference instantaneous intensity of  $10^{12}$  W/m<sup>2</sup>. The one-plasmon decay rates are independent of intensity and the two-plasmon decay rates increase proportionally with intensity. The geometries affect the instantaneous electric field and hence the relative contributions of one and two-plasmon processes: the left panels show results for a roughened metal surface assuming ideal coupling, the center panels for a 20 nm sphere and the right panels for a 100 nm sphere.

of frequency for the four plasmonic metals considered above. Results are shown per incident photon for a reference intensity of  $10^{12}$  W/m<sup>2</sup>, which corresponds, for example, to a 100 nJ pulse with width 100 fs focused to a 1 mm<sup>2</sup> spot size. The one-plasmon contribution per photon is independent of light intensity (linear response), whereas the two-plasmon contribution per photon increases linearly with light intensity. For the ideal coupling slab at this reference intensity, the two-plasmon process is consistently 3–4 orders of magnitude weaker than the one-plasmon process, with a weak frequency dependence of this ratio for all four metals. For the spheres, the ratio varies much more with frequency and peaks at the localized surface plasmon resonance frequency, where the electric field intensity inside the metal is strongest. Note that the two-plasmon process would dominate over the one-plasmon process in any of these metals or geometries only for an instantaneous pulse intensity that is 4 orders of magnitude larger, that is,  $\sim 10^{16}$  W/m<sup>2</sup>.

## METHODS

We calculate electronic band structures, wave functions and optical matrix elements of the plasmonic metals, gold, silver, copper and aluminum, using the open-source plane-wave density-functional theory software, JDFTx.<sup>43</sup> These calculations

employ norm-conserving pseudopotentials, a 30 hartree kinetic energy cutoff on the plane-wave basis, and the PBEsol<sup>44</sup> generalized gradient approximation for the exchange-correlation functional, with a rotationally invariant + *U* correction<sup>45</sup> for localized *d* electrons. All calculations are fully relativistic, accounting for spin–orbit effects self-consistently, which is essential for accurately reproducing the quasiparticle band structure in agreement with photoemission measurements.<sup>37</sup>

We additionally calculate the phonon band structures and electron–phonon matrix elements (which accurately predict electrical resistivities of metals within 5%<sup>36</sup>) and recast all electron and phonon properties in a basis of localized Wannier functions.<sup>46</sup> We then evaluate the matrix elements for arbitrary Feynman diagrams involving electron–light and electron–phonon interactions using the Wannier-basis Hamiltonian to interpolate to arbitrary wave-vectors in the Brillouin zone. This enables us to evaluate integrals over the Brillouin zone in the Fermi Golden rule for various processes (direct and phonon-assisted, one- and two-plasmon decays, eqs 1–4) using a dense Monte Carlo sampling with  $\sim 10^7$  points. See ref 36 for details of the Wannier formulation of electron–phonon–optical diagrams and details of the Wannier and phonon calculations.

## DISCUSSION AND CONCLUSIONS

We examine nonlinear losses in metals using ab initio electronic structure calculations and predict the relative contributions and carrier energy distributions from one and two-plasmon decay. We show that the contribution of two-plasmon decay ( $\text{Im } \chi^3$ ) becomes comparable to that of one-plasmon decay ( $\text{Im } \chi^1$ ) only at instantaneous incident light intensities  $\sim 10^{16}$  W/m<sup>2</sup>, both for surface plasmon polaritons and localized surface plasmons. Geometry affects the relative contributions by changing the ratio of the average  $E^4$  and  $E^2$ , where  $E(\mathbf{r})$  is the electric field inside the metal. This electric field can be enhanced somewhat in sharp geometries, for example, by focusing surface plasmon polaritons,<sup>47</sup> but plasmonic field enhancement primarily boosts the field outside the metal.

Experimentally accessing the regime where two-plasmon decay dominates, by increasing the incident intensity by shaping the pulse either in time or space (focusing) is challenging because the absorbed power density will rapidly destroy the material. For example in gold at 2 eV, where the two/one-plasmon contribution ratio peaks assuming ideal coupling (Figure 4), the electric field at which this ratio becomes unity is  $\sim 10^{-3}$  au (Figure 2). At this field intensity, the total absorbed power per unit volume in the material  $\sim 10^{-8}$  au  $\sim 10^{22}$  W/m<sup>3</sup>. Given that  $\sim 10^9$  J/m<sup>3</sup> is sufficient to melt gold,<sup>48</sup> this necessitates that the incident light be restricted to  $\sim 10^{-13}$  s, that is, 100 fs. Therefore, accessing the two-plasmon dominant regime before melting the particle is at the limit of current pulsed laser measurements. This makes it particularly unlikely that multiplasmon cooperative decay processes play any significant role in hot carrier generation at continuous-wave solar intensities, and we expect plasmonic catalysis to remain in the domain of conventional single-plasmon decay processes.

Instead, we propose that practical signatures of the two-plasmon decay process employ the carriers generated from the decay. These carriers carry energy up to twice the maximum energy of those generated from conventional single-plasmon decay, and can potentially access semiconductor bands or molecule energy levels that are inaccessible to the dominant lower order decay. The carrier distribution predictions of this work, as shown in Figure 3, can therefore guide the design of

plasmon-enhanced Raman or photoluminescence measurements that utilize up-converted carriers from multiplasmon decay.

Future extensions of this work to explicitly account for confinement effects would be useful to examine the possibility of enhancing two-plasmon carrier generation in small metal nanostructures. We expect the dominant effect to be alteration of the electron-plasmon matrix element to include intraband transitions (since crystal momentum conservation is no longer required), in addition to alterations of the electron and phonon density of states. Experimental design for ultraconfined geometries will also need to carefully account for competing quadratic nonlinearity processes at the surface, but these cannot generate up-converted carriers, which we believe will remain the key to detect and exploit the cubic-nonlinearity two-plasmon decay process.

## AUTHOR INFORMATION

### Corresponding Authors

\*E-mail: [prineha@caltech.edu](mailto:prineha@caltech.edu). Ph.:(215) 882-0385.

\*E-mail: [shankars@caltech.edu](mailto:shankars@caltech.edu). Ph.:(607) 379-3473.

\*E-mail: [haa@caltech.edu](mailto:haa@caltech.edu).

### Author Contributions

<sup>†</sup>These authors contributed equally (P.N. and R.S.).

### Notes

The authors declare no competing financial interest.

## ACKNOWLEDGMENTS

This material is based on work performed by the Joint Center for Artificial Photosynthesis, a DOE Energy Innovation Hub, supported through the Office of Science of the U.S. Department of Energy under Award Number DE-SC0004993. P.N. is supported by a National Science Foundation Graduate Research Fellowship and by the Resnick Sustainability Institute. A.S.J. acknowledges support from the Barry M. Goldwater Scholarship. The authors acknowledge support from NG NEXT at Northrop Grumman Corporation. Calculations in this work used the National Energy Research Scientific Computing Center, a DOE Office of Science User Facility supported by the Office of Science of the U.S. Department of Energy under Contract No. DE-AC02-05CH11231.

## REFERENCES

- (1) Barnes, W. L.; Dereux, A.; Ebbesen, T. W. Surface Plasmon Subwavelength Optics. *Nature* **2003**, *424*, 824–830.
- (2) Chang, D. E.; Sorensen, A. S.; Hemmer, P. R.; Lukin, M. D. Quantum Optics with Surface Plasmons. *Phys. Rev. Lett.* **2006**, *97*, 053002.
- (3) Atwater, H. A.; Polman, A. Plasmonics for Improved Photovoltaic Devices. *Nat. Mater.* **2010**, *9*, 205–213.
- (4) Elson, J. M.; Ritchie, R. H. Photon Interactions at a Rough Metal Surface. *Phys. Rev. B* **1971**, *4*, 4129–4138.
- (5) Wang, F. X.; Rodríguez, F. J.; Albers, W. M.; Ahorinta, R.; Sipe, J. E.; Kauranen, M. Surface and Bulk Contributions to the Second-Order Nonlinear Optical Response of a Gold Film. *Phys. Rev. B: Condens. Matter Mater. Phys.* **2009**, *80*, 233402.
- (6) Palomba, S.; Novotny, L. Nonlinear Excitation of Surface Plasmon Polaritons by Four-Wave Mixing. *Phys. Rev. Lett.* **2008**, *101*, 056802.
- (7) Owens, D. T.; Fuentes-Hernandez, C.; Hales, J. M.; Perry, J. W.; Kippelen, B. A Comprehensive Analysis of the Contributions to the Nonlinear Optical Properties of Thin Ag Films. *J. Appl. Phys.* **2010**, *107*, 123114.
- (8) Nahata, A.; Linke, R. A.; Ishi, T.; Ohashi, K. Enhanced Nonlinear Optical Conversion From A Periodically Nanostructured Metal Film. *Opt. Lett.* **2003**, *28*, 423–425.
- (9) Lepeshkin, N. N.; Schweinsberg, A.; Piredda, G.; Bennink, R. S.; Boyd, R. W. Enhanced Nonlinear Optical Response of One-Dimensional Metal-Dielectric Photonic Crystals. *Phys. Rev. Lett.* **2004**, *93*, 123902.
- (10) MacDonald, K. F.; Samson, Z. L.; Stockman, M. I.; Zheludev, N. I. Ultrafast Active Plasmonics. *Nat. Photonics* **2009**, *3*, 55–58.
- (11) Clavero, C. Plasmon-Induced Hot-Electron Generation at Nanoparticle/Metal-Oxide Interfaces for Photovoltaic and Photocatalytic Devices. *Nat. Photonics* **2014**, *8*, 95–103.
- (12) Linic, S.; Christopher, P.; Ingram, D. B. Plasmonic-Metal Nanostructures for Efficient Conversion of Solar to Chemical Energy. *Nat. Mater.* **2011**, *10*, 911–921.
- (13) Leenheer, A. J.; Narang, P.; Lewis, N. S.; Atwater, H. A. Solar Energy Conversion via Hot Electron Internal Photoemission in Metallic Nanostructures: Efficiency Estimates. *J. Appl. Phys.* **2014**, *115*, 134301.
- (14) Narang, P.; Sundararaman, R.; Atwater, H. A. Plasmonic Hot Carrier Dynamics in Solid-State and Chemical Systems for Energy Conversion. *Nanophotonics* **2016**, *5*, 96.
- (15) Frontiera, R. R.; Henry, A.-I.; Gruenke, N. L.; Van Duyne, R. P. Surface-Enhanced Femtosecond Stimulated Raman Spectroscopy. *J. Phys. Chem. Lett.* **2011**, *2*, 1199–1203.
- (16) Dieringer, J. A.; Lettan, R. B.; Scheidt, K. A.; Van Duyne, R. P. A Frequency Domain Existence Proof of Single-Molecule Surface-Enhanced Raman Spectroscopy. *J. Am. Chem. Soc.* **2007**, *129*, 16249–16256.
- (17) Ringe, E.; McMahon, J. M.; Sohn, K.; Cogley, C.; Xia, Y.; Huang, J.; Schatz, G. C.; Marks, L. D.; Van Duyne, R. P. Unraveling the Effects of Size, Composition, and Substrate on the Localized Surface Plasmon Resonance Frequencies of Gold and Silver Nanocubes: A Systematic Single-Particle Approach. *J. Phys. Chem. C* **2010**, *114*, 12511–12516.
- (18) Babicheva, V. E.; Zhukovsky, S. V.; Ikhsanov, R. S.; Protsenko, I. E.; Smetanin, I. V.; Uskov, A. Hot Electron Photoemission from Plasmonic Nanostructures: The Role of Surface Photoemission and Transition Absorption. *ACS Photonics* **2015**, *2*, 1039–1048.
- (19) Govorov, A. O.; Zhang, H.; Demir, H. V.; Gun'ko, Y. K. Photogeneration of Hot Plasmonic Electrons with Metal Nanocrystals: Quantum Description and Potential Applications. *Nano Today* **2014**, *9*, 85–101.
- (20) Zhang, H.; Govorov, A. O. Optical Generation of Hot Plasmonic Carriers in Metal Nanocrystals: The Effects of Shape and Field Enhancement. *J. Phys. Chem. C* **2014**, *118*, 7606–7614.
- (21) Harutyunyan, H.; Martinson, A. B. F.; Rosenmann, D.; Khorashad, L. K.; Besteiro, L. V.; Govorov, A. O.; Wiederrecht, G. P. Anomalous Ultrafast Dynamics of Hot Plasmonic Electrons in Nanostructures with Hot Spots. *Nat. Nanotechnol.* **2015**, *10*, 770–774.
- (22) Mukherjee, S.; Libisch, F.; Large, N.; Neumann, O.; Brown, L. V.; Cheng, J.; Lassiter, J. B.; Carter, E. A.; Nordlander, P.; Halas, N. J. Hot Electrons Do the Impossible: Plasmon-Induced Dissociation of H<sub>2</sub> on Au. *Nano Lett.* **2013**, *13*, 240–247.
- (23) Cushing, S. K. Photocatalytic Activity Enhanced by Plasmonic Resonant Energy Transfer from Metal to Semiconductor. *J. Am. Chem. Soc.* **2012**, *134*, 15033–15041.
- (24) Scalora, M.; Vincenti, M. A.; de Ceglia, D.; Roppo, V.; Centini, M.; Akozbek, N.; Bloemer, M. J. Second- and Third-Harmonic Generation in Metal-Based Structures. *Phys. Rev. A: At, Mol., Opt. Phys.* **2010**, *82*, 043828.
- (25) Smith, D. D.; Yoon, Y.; Boyd, R. W.; Campbell, J. K.; Baker, L. A.; Crooks, R. M.; George, M. Z-Scan Measurement of the Nonlinear Absorption of a Thin Gold Film. *J. Appl. Phys.* **1999**, *86*, 6200–6205.
- (26) O'Donnell, K. A.; Torre, R. Characterization of the Second-Harmonic Response of a Silver/Air Interface. *New J. Phys.* **2005**, *7*, 154.
- (27) Zheludev, N. I.; Bennett, P. J.; Loh, H.; Popov, S. V.; Shatwell, I. R.; Svirko, Y. P.; Gusev, V. E.; Kamalov, V. F.; Slobodchikov, E. V.

Cubic Optical Nonlinearity of Free Electrons in Bulk Gold. *Opt. Lett.* **1995**, *20*, 1368.

(28) Vincenti, M. A.; de Ceglia, D.; Ciattoni, A.; Scalora, M. Singularity-Driven Second- and Third-Harmonic Generation at  $\epsilon$ -Near-Zero Crossing Points. *Phys. Rev. A: At, Mol., Opt. Phys.* **2011**, *84*, 063826.

(29) Ignatyeva, D. O.; Sukhorukov, A. P. Femtosecond-Pulse Control in Nonlinear Plasmonic Systems. *Phys. Rev. A: At, Mol., Opt. Phys.* **2014**, *89*, 013850.

(30) Zeng, Y.; Hoyer, W.; Liu, J.; Koch, S. W.; Moloney, J. V. Classical Theory for Second-Harmonic Generation from Metallic Nanoparticles. *Phys. Rev. B: Condens. Matter Mater. Phys.* **2009**, *79*, 235109.

(31) Cao, L.; Panoiu, N. C.; Bhat, R. D. R.; Osgood, R. M. Surface Second-Harmonic Generation from Scattering of Surface Plasmon Polaritons from Radially Symmetric Nanostructures. *Phys. Rev. B: Condens. Matter Mater. Phys.* **2009**, *79*, 235416.

(32) Huang, J.; Wang, W.; Murphy, C. J.; Cahill, D. G. Resonant Secondary Light Emission from Plasmonic Au Nanostructures at High Electron Temperatures Created by Pulsed-Laser Excitation. *Proc. Natl. Acad. Sci. U. S. A.* **2014**, *111*, 906–911.

(33) Bouhelier, A.; Beversluis, M. R.; Novotny, L. Characterization of Nanoplasmonic Structures by Locally Excited Photoluminescence. *Appl. Phys. Lett.* **2003**, *83*, 5041–5043.

(34) Biagioni, P.; Brida, D.; Huang, J.-S.; Kern, J.; Duò, L.; Hecht, B.; Finazzi, M.; Cerullo, G. Dynamics of Four-Photon Photoluminescence in Gold Nanoantennas. *Nano Lett.* **2012**, *12*, 2941–2947.

(35) Brown, A. M.; Sundararaman, R.; Narang, P.; Goddard, W. A., III; Atwater, H. A. Ab Initio Phonon Coupling and Optical Response of Hot Electrons in Plasmonic Metals. *preprint arXiv:1602.00625* **2016**.

(36) Brown, A. M.; Sundararaman, R.; Narang, P.; Goddard, W. A., III; Atwater, H. A. Non-Radiative Plasmon Decay and Hot Carrier Dynamics: Effects of Phonons, Surfaces and Geometry. *ACS Nano* **2016**, *10*, 957.

(37) Sundararaman, R.; Narang, P.; Jermyn, A. S.; Goddard, W. A., III; Atwater, H. A. Theoretical Predictions for Hot-Carrier Generation from Surface Plasmon Decay. *Nat. Commun.* **2014**, *5*, 5788.

(38) Palik, E. D. *Handbook of Optical Constants of Solids*; Academic: New York, 1985.

(39) Marini, A.; Onida, G.; Del Sole, R. Quasiparticle Electronic Structure of Copper in the GW Approximation. *Phys. Rev. Lett.* **2001**, *88*, 016403.

(40) Marini, A.; Del Sole, R.; Onida, G. First-Principles Calculation of the Plasmon Resonance and of the Reflectance Spectrum of Silver in the GW Approximation. *Phys. Rev. B: Condens. Matter Mater. Phys.* **2002**, *66*, 115101.

(41) Mie, G. Beiträge zur Optik trüber Medien, speziell kolloidaler Metallösungen. *Ann. Phys.* **1908**, *330*, 377–445.

(42) Matzler, C. *MATLAB Functions for Mie Scattering and Absorption*; Institut für Angewandte Physik, 2002

(43) Sundararaman, R.; Gunceler, D.; Letchworth-Weaver, K.; Arias, T. A. JDFTx; <http://jdfx.sourceforge.net>, 2012 (accessed Oct 6, 2015, code revision #1166).

(44) Perdew, J. P.; Ruzsinszky, A.; Csonka, G. I.; Vydrov, O. A.; Scuseria, G. E.; Constantin, L. A.; Zhou, X.; Burke, K. Restoring the Density-Gradient Expansion for Exchange in Solids and Surfaces. *Phys. Rev. Lett.* **2008**, *100*, 136406.

(45) Dudarev, S. L.; Botton, G. A.; Savrasov, S. Y.; Humphreys, C. J.; Sutton, A. P. Electron-Energy-Loss Spectra and the Structural Stability of Nickel Oxide: An LSDA+U Study. *Phys. Rev. B: Condens. Matter Mater. Phys.* **1998**, *57*, 1505–1509.

(46) Souza, I.; Marzari, N.; Vanderbilt, D. Maximally Localized Wannier Functions for Entangled Energy Bands. *Phys. Rev. B: Condens. Matter Mater. Phys.* **2001**, *65*, 035109.

(47) Giugni, A.; Torre, B.; Toma, A.; Francardi, M.; Malerba, M.; Alabastri, A.; Zaccaria, R. P.; Stockman, M. I.; Fabrizio, E. D. Hot-Electron Nanoscopy using Adiabatic Compression of Surface Plasmons. *Nat. Nanotechnol.* **2013**, *8*, 845.

(48) Lide, D. *CRC Handbook of Chemistry and Physics*, 84th ed.; Taylor & Francis, 2003.